Clim. Past Discuss., 9, 5123–5156, 2013
www.clim-past-discuss.net/9/5123/2013/
doi:10.5194/cpd-9-5123-2013

Climate of the Past Discussions
Open Access

Seasonal changes in glacial polynya activity inferred from Weddell Sea varves

D. Sprenk[1], M. E. Weber[1], G. Kuhn[2], V. Wennrich[1], T. Hartmann[1], and K. Seelos[3]

[1]University of Cologne, Institute of Geology and Mineralogy, Cologne, Germany
[2]Alfred-Wegener-Institut Helmholtz-Zentrum für Polar- und Meeresforschung, Bremerhaven, Germany
[3]Johannes Gutenberg University Mainz, Institute of Geosciences, Mainz, Germany

Received: 15 August 2013 – Accepted: 22 August 2013 – Published: 6 September 2013

Correspondence to: D. Sprenk (danielasprenk@gmail.com)

Published by Copernicus Publications on behalf of the European Geosciences Union.

Abstract

The Weddell Sea and the associated Filchner-Rønne Ice Shelf constitute key regions for global bottom-water production today. However, little is known about bottom-water production under different climate and ice-sheet conditions. Therefore, we studied core PS1795, which consists primarily of fine-grained siliciclastic varves that were deposited on contourite ridges in the southeastern Weddell Sea during the Last Glacial Maximum (LGM). We conducted high-resolution X-ray fluorescence (XRF) analysis and grain-size measurements with the RADIUS tool (Seelos and Sirocko, 2005) using thin sections to characterize the two seasonal components of the varves at sub-mm resolution to distinguish the seasonal components of the varves.

Bright layers contain coarser grains that can mainly be identified as quartz in the medium to coarse silt grain size. They also contain higher amounts of Si, Zr, Ca, and Sr, as well as more ice-rafted debris (IRD). Dark layers, on the other hand, contain finer particles such as mica and clay minerals from the chlorite and illite groups. In addition, chemical elements, Fe, Ti, Rb, and K are elevated as well. Based on these findings as well as on previous analyses on neighbouring cores, we propose a model of glacially enhanced thermohaline convection in front of a grounded ice sheet that is supported by seasonally variable coastal polynya activity. Accordingly, katabatic (i.e. offshore blowing) winds removed sea ice from the ice edge, leading to coastal polynya formation. We suggest that glacial processes were similar to today with stronger katabatic winds and enhanced coastal polynya activity during the winter season. If this is correct, silty layers are likely glacial winter deposits, when brine rejection was increased, leading to enhanced bottom water formation and increased sediment transport. Vice versa, finer-grained clayey layers were then deposited during summer, when coastal polynya activity was likely reduced.

CPD
9, 5123–5156, 2013

1 Introduction

The Weddell Sea is a key region for Earth's climate variability because it influences global thermohaline circulation (Seidov et al., 2001; Rahmstorf, 2002) as one of the major sites of deep- and bottom-water formation (Huhn et al., 2008). The present-day bottom-water formation, which is rather well known, requires flow and mixing of water masses underneath the Filchner-Rønne Ice Shelf and brine release within polynyas on the southern Weddell Sea shelf to form cold and dense water masses that can flow across the shelf and into the deep Weddell Basin (see chapter Oceanography).

However, little is known about glacial bottom-water production although Antarctica may have acted as a major supplier of deep water, i.e. Antarctic Bottom Water (AABW) during stadials (Shin et al., 2003), when production of North Atlantic Deep Water (NADW) was sluggish or even terminated (e.g. Stocker and Johnson, 2003; Knutti et al., 2004). Glacial times did not involve major floating ice shelves. Specifically during the Last Glacial Maximum (LGM) from 26.5–19 ka before present (BP) (Clark et al., 2009) most ice sheets were grounded and had advanced close to or even reached the shelf edge. In the Weddell Sea, during the LGM the ice sheet at least advanced very close, i.e. within 40 km (Larter et al., 2012) to the shelf edge and most likely even reached it (Weber et al., 2011; Elverhøi, 1984; Larter et al., 2012; Hillenbrand et al., 2012). Therefore, glacial bottom-water must have been produced very differently as ice shelf cavities required for supercooling High-Salinity Shelf Water (HSSW) to produce Ice-Shelf Water (ISW) would be inexistent (Gales et al., 2012). Here, we will provide a conceptual model of glacial brine rejection in coastal polynyas that led to intense thermohaline convection in front of a grounded ice sheet as a possible model for glacial bottom-water production.

Earlier studies (e.g. Weber et al., 1994, 2010, 2011; Sprenk et al., 2013b) of the channel-ridge system located on a terrace of the continental slope in the southeastern Weddell Sea (Fig. 1) have revealed that the laminated deposits represent true varves formed by seasonal variations in thermohaline convection during the LGM. Recently,

CPD
9, 5123–5156, 2013

Sprenk et al. (2013b) investigated decadal-scale oscillations including a persistent 50–85 yr cycle in varve thickness data of three cores originating from the northeastern prolongation of the channel-ridge-system. Accordingly, decadal-scale fluctuations in sedimentation rates are consistent with periods of solar cycles during the LGM, e.g. the Gleissberg (Gleissberg, 1944, 1958) cycle and are therefore indirectly related to changes in total solar irradiance.

To obtain detailed information on the internal structure of the varves on a seasonal scale, we investigated gravity core PS1795 from the same channel-ridge-system and analysed sediment-physical properties. We gained detailed insight on the chemical composition and the grain size variation of the varves using high-resolution X-ray fluorescence (XRF)-scanner and RADIUS tool (Seelos and Sirocko, 2005) data every 0.2 mm.

During the LGM and the last glacial transition while the East Antarctic Ice Sheet advanced to the shelf break, coastal polynyas were active above the continental slope, which induced brine rejection and therefore high-salinity water production (Weber et al., 2011). These dense water masses reworked sediment and drained into the channels, depositing the material mainly northwest of each channel because of the Coriolis force, building natural levees (Michels et al., 2002). Depending on seasonal velocity changes of the thermohaline current, the transporting sediment grain size changed, leading to varved sedimentation with alternating silty-rich and more clayey layers. Bioturbated hemipelagic mud was deposited during times, when the ice sheet was retreated from the shelf edge and sea ice was reduced. The velocity of the thermohaline current is strongly decreased, leading to significantly lower linear sedimentation rates. The final East Antarctic Ice Sheet retreat was around 16 ka, marked by a transition from laminated to bioturbated sedimentation at every core site (Weber et al., 2011).

CPD
9, 5123–5156, 2013

2 Study area and regional oceanography

We study gravity cores originating from the southeastern Weddell Sea, which were retrieved with R/V Polarstern (PS) in the late 1980s and early 1990s (Fig. 1). The core sites are located in channel-ridge systems on a terrace of the continental slope in 1900–3139 m water depth. Each ridge is up to 300 m high and up to 100 km long and runs parallel, on the northwestern side of a channel (e.g. Weber et al., 1994; Kuhn and Weber, 1993).

The Weddell Sea is the southernmost part of the Atlantic sector of the Southern Ocean. The South Scotia Ridge marks the northern boundary and in the east it is limited by the Coats Land and Dronning Maud Land, where smaller ice shelves like the Brunt and Riiser-Larsen Ice Shelf are located offshore (Fig. 1). The southern Weddell Sea is covered by the Filchner-Rønne Ice Shelf. In the west the Antarctic Peninsula borders the Weddell Sea.

About 60 % (Orsi et al., 1999) to 70 % (Carmack and Foster, 1977) of the Antarctic Bottom Water (AABW) originates from the Weddell Sea, where Weddell Sea Bottom Waters (WSBW) is produced (Huhn et al., 2008; Foldvik et al., 2004). Maldonado et al. (2005) even argued that 80 % of AABW is produced in the Weddell Sea by brine rejection and supercooling.

Cyclonic movement of all water masses within the Weddell Gyre dominates the Weddell Sea circulation (Fig. 1). Relatively warm Circumpolar Deep Water (CDW) is transported by the Weddell Gyre from the Antarctic Circumpolar Current (ACC) southwards along the eastern boundary into the Weddell Sea and mixes with cold surface waters generating Warm Deep Water (WDW) (e.g. Orsi et al., 1993; Gordon et al., 2010). Through heat loss and mixing primarily during winter with Winter Water (WW) while flowing further to the West along the continental margin, WDW becomes Modified Warm Deep Water (MWDW). MWDW intrudes onto the shelf and mixes with the ISW to produce WSBW (Foldvik et al., 1985). HSSW is being generated during sea ice production by brine rejection (Foldvik et al., 2004; Petty et al., 2013) and is then

CPD
9, 5123–5156, 2013

supercooled by circulation under the ice shelf becoming dense Ice-Shelf Water (ISW; Nicholls et al., 2009). Passive tracer experiments also point to the Filchner-Rønne Ice Shelf as the main location for bottom water production (Beckmann et al., 1999).

Bottom-water drainage is across the over-deepened Filchner Trough along the south-north running channel-ridge systems into the Weddell Basin (Fig. 1). There, it is deflected to the left due to Coriolis Force and flows clockwise along the continental slope within the Weddell Gyre (Foldvik, 1986). Although a current meter mooring (AWI-213) in the northeastern prolongation of the channel-ridge systems investigated here, still shows a near-bottom flow underneath the Weddell Gyre with a predominant northeastern direction (Weber et al., 1994).

3 Methods

Gravity core PS1795 was opened and splitted into archive and working halves at the laboratory of the Alfred Wegener Institute in Bremerhaven. All sampling was accomplished on working halves, while sediment physical properties were measured non-destructively at 1 cm increments on full round cores and archive halves. We used the GEOTEK Multi-Sensor-Core Logger (MSCL; method see Weber et al., 1997) for determining wet-bulk density (WBD), compression wave velocity (Vp) as well as magnetic susceptibility (MS). For MS measurements a Bartington point sensor (MS2F) was used and the data was volume-corrected. Also L*, a*, and b* colour components (Weber, 1998) were measured, using a Minolta spectrophotometer CM-2002. L* gives information about the sediment lightness, colour a* reflects the amount of green-red, and colour b* is the blue-yellow component.

Water content was estimated on sediment samples every 5 cm by freeze-drying. Information about the geochemical composition was gained by analysing bulk samples with an element analyser. Contents of total carbon (TC), inorganic carbon (TIC), and organic carbon (TOC; TIC subtracted from TC), as well as total nitrogen (TN) and total sulphur (TS) were measured. We also determined biogenic opal contents by leaching

CPD
9, 5123–5156, 2013

with 1M NaOH-solution according to the method see Müller and Schneider (1993). All resulting bulk data have been corrected for the containing amount of sea salt in the pore fluid (35 ‰).

To analyse sediment fabric, we cut out 1 cm thick, 10 cm wide, and 25 cm long plates from the centre of each core using a double-bladed saw. The plates were exposed for 3 to 5 min to a HP 43855 X-Ray System. After scanning the negatives at 300 dots per inch (dpi) resolution, we adjusted brightness and contrast to enable a better distinction of dark and bright layers, which are only a few millimetres thick.

Additionally we counted all grains > 1 mm and > 2 mm in diameter, reflecting ice-rafted debris (IRD). To do that, we used the scanned X-radiographs and place a semi-transparent 1 × 1 mm grid onto it; for further information on the method see Grobe (1987).

To obtain information on the distribution of chemical elements we measured the sediment cores non-destructively at 1 cm resolution using an Avaatech XRF core scanner (Jansen et al., 1998) at the Alfred Wegener Institute in Bremerhaven. For high-resolution element analysis, XRF-scanning was carried out every 0.2 mm on three consecutive split sediment core sections (197–499 cm) of PS1795 using a 3.0 kW Molybdenum tube. For these measurements, the ITRAX XRF-scanner (Cox Analytical, Sweden), a multi-function instrument for non-destructive optical, radiographic, and chemical elemental sediment core analyses (Croudace et al., 2006), was used at the Cologne University laboratory. We also used the ITRAX scanner equipped with a 1.9 kW Chromium tube, to produce X-radiographs of the archive halves.

For accelerator mass spectrometry (AMS) radiocarbon dating we used well-preserved carbonate shell material originating from planktonic foraminifera *Neogloboquadrina pachyderma* (sinistral). Beforehand, H_2O_2 was added to each sample to remove the organic material. All measurements were conducted at the ETH laboratory of Ion Beam Physics in Zurich. AMS ^{14}C ages were reservoir corrected (1.215 ± 30 yr; see Weber et al., 2011), based on age dating of carbonate shell material from a living bryozoa from neighbouring Site PS1418-1 (Melles, 1991). Clam version 2.1 (Blaauw,

CPD
9, 5123–5156, 2013

2010) and Marine09 calibration curve (Reimer et al., 2011) were applied to calibrate the AMS ^{14}C of PS1795 and calculate calendar ages (Table 1). We used a cubic spline age-depth model with the weighted average of 10 000 iterations with 95 % confidence range.

We also produced two overlapping thin sections (PS1795: 354.6–373.2 cm; 371.5–381.2 cm) for a detailed analysis of individual layers. Therefore, aluminium boxes were pressed into the sediment and then sliced with a fishing line. After carefully removing the sediment slabs from the core half, samples were immediately flash-freezed in liquid nitrogen and then freeze-dried. Slabs were then embedded in epoxy resin under vacuum and cured afterwards. For more details on the method see Cook et al. (2009) and Francus and Asikainen (2001). To obtain thin sections, the dried epoxy-impregnated sediment slabs were cut, grinded, and polished to a thickness of only a few millimetres. The thin sections were also scanned using the ITRAX system at the University of Cologne at 0.2 mm-resolution as well as scanned with a flatbed scanner for negative transparency scanning.

Additionally, we applied the RADIUS tool, providing rapid particle analysis of digital images by ultra-high resolution scanning of thin sections (Seelos and Sirocko, 2005), which uses the commercial image processing software analySIS (Soft Imaging System GmbH) controlled by three macro-scripts by Seelos (2004). Thin sections were therefore scanned on a fully-automatic polarization microscope in combination with a digital microscope camera at the University of Mainz. The scripts derive mineral-specific particle-size distributions that cover grain sizes from medium silt to coarse sand. The RADIUS tool was used on the thin sections (PS1795: 354.6–373.2 cm; 371.5–381.2 cm) at 100 µm-resolution.

For automatic layer recognition and counting we used the BMPix and PEAK tool (Weber et al., 2010). First, grey values were extracted from the scanned X-radiographs using the BMPix tool. Then, the PEAK tool was used to count every maximum, i.e. bright layers, every minimum, i.e. dark layers, or every transition of the grey scale curve. For more precise counting results we manually examined and revised all counting results

CPD
9, 5123–5156, 2013

generated by the PEAK tool. See Sprenk et al. (2013b) for further information about the counting method, its uncertainties, and discrepancy estimations.

4 Results

4.1 Sediment-physical data

The 8.99 m long gravity core PS1795 (74°30′ S, 28°11′ W, 1884 m water depth) is located southwest of the southern sediment ridge (Fig. 1). Sediments are relatively homogenous grey to brown (Fig. 2a), only the uppermost 23 cm are yellow to orange-brown due to oxidation. Analyses of the coarse grain fraction (> 63 µm) of PS1795 every five centimetres shows that the main components of the coarse grains are quartz (80 % on average), but also feldspars, biotite, and hornblende make up 3–5 % each. Overall, maxima in MS (Fig. 2c) correlate with high high IRD counts (Fig. 2b).

From 2.15 m to the bottom of the core at 8.99 m, sediment is mostly laminated, consisting of alternating clayey and silty layers, each only up to a few millimetre thick. Laminated sediment consists mainly of terrigenous material with only 2–6 % biogenic opal, less than 0.2 % TIC/TOC, and about 0.04 % TN. WBD vary only slightly from 1.8 to 2.0 g cm^{-3}. IRD content shows relatively strong fluctuations in the laminated sediment and varies between 0–18 grains cm^{-2} (Fig. 2).

Between 6.42–6.87 m the sediment is nearly structureless, showing no bioturbation or laminations and contains only few IRD (Fig. 2b). Sediment-physical properties, e.g. MS, water content, and WBD of the 45 cm long section show only marginal fluctuations, suggesting a very homogenous composition.

A 3 cm thick coarse sand layer is intercalated into laminated sediment at 6.21 m, which is also reflected in sediment-physical properties. The coarse sand layer shows maxima in MS, IRD content, and WBD as well as minima in water content, TN, biogenic opal, Si, and Fe (Fig. 2).

CPD
9, 5123–5156, 2013

The uppermost 2.15 m of PS1795 are characterized by highly bioturbated mud with varying IRD-content. The transition from laminated to bioturbated sediment is clearly documented in all parameters (Fig. 2). Water contents rise significantly from about 30 to 40 %, colour a* drops slightly, and WBD decreases to $\sim 1.6\,g\,cm^{-3}$. Overall, bioturbated sediment shows higher TOC, TIC, TN, and biogenic opal values than laminated sediment, indicating higher bioproductivity. Between 0.37–0.48 m bioturbated sediment contains high amount of IRD as well as the highest TOC contents and the lowest biogenic opal values.

To form bioturbated sediment requires low sedimentation rates and at least partly open-water conditions (reduced sea-ice cover). Accordingly, bioturbated sediment was most likely deposited during times, when the ice sheet was retreated from the shelf edge (e.g. Weber et al., 1994, 2011). Therefore, the dense water masses are formed on the southern Weddell Sea shelf as today (see Oceanography section). Accordingly, due to the retreated ice sheet less ice-transported sediment was deposited on the upper slope.

4.2 Chronology

Using sediment slices up to 25 cm thick and labour-intense microscopic analysis, we managed to collect enough intact shell material from planktonic foraminifera *Neogloboquadrina pachyderma* for six AMS^{14}C analyses (Table 1). Three samples have less than 0.3 mg C, which is close to the detection limit of radiocarbon dating possible at ETH Zurich. Two of those samples show slight age reversals relative to those with greater amounts of C, and are therefore not included in the final age models. Nonetheless, the error range of AMS^{14}C age of 24.19 ± 0.29 ka at 6.68 m depth lies within the age range of the age-depth-models and is possibly caused by high linear sedimentation rates of about $1.1–1.6\,m\,kyr^{-1}$ (Fig. 6).

We constructed two different age-depth-models for the sediment core PS1795. One age-model for undisturbed sedimentation relying only on the AMS^{14}C ages plus an age-depth-model, which includes a hiatus at a core depth of about 2.15 m. The X-

CPD
9, 5123–5156, 2013

radiograph highlights an erosive contact between laminated and bioturbated sediment at 2.15 m (Fig. 2) and also the varve counting results lead to the assumption that sedimentation is disturbed at the base of the bioturbated section. However, it is not possible to count the varves accurately between 2.15 and 2.57 m due to the low quality of the X-radiographs, the material can be identified as varved sediment. Nonetheless, based on the visually detectable faint lamination, the material can be considered varves. Using an estimated LSR of approximately 1.1–1.6 m kyr^{-1} the varved sediment possibly includes about 260–380 varves, which gives an age for the top of the varved sediments between 21.8 and 22.4 ka. The topmost 2.15 m, cover about the last 17–18 kyr as the AMS^{14}C age of 17.44 ± 0.36 ka close to the base of the bioturbated section reveals. This reflects linear sedimentation rates of only 0.12 m kyr^{-1} for the bioturbated sediment. Accordingly, the combination of varve counting and radiocarbon dating strongly suggests incomplete sedimentation, with a hiatus of approximately 3 to 4 kyr (Fig. 2).

4.3 Varves

The varve character of the laminations has been established in earlier studies (Weber et al., 1994, 2010a, 2011; Sprenk et al., 2013b). The most convincing argument is provided by core PS1789 (location see Fig. 1), which yields the visually most complete record of LGM varvation. Two horizons at 199 cm and 1211 cm core depth date to 19.223 and 22.476 ka, respectively. Over this age difference of 3253 yr (± 529 yr), we counted 3329 laminae couplets (see Fig. 8 of Weber et al., 2010) – a very convincing and robust indication of the seasonal nature of the lamination. The ^{14}C ages and varve counting results of PS1795 of this study also approve the seasonal sedimentation (see following sections).

In this study, analyses concentrate on laminated sections of newly opened core PS1795. Accordingly, the density of the coarser layers is slightly higher, leading to less darkening of the X-ray film (Axelsson, 1983), therefore X-radiographs have been successfully used for varve counting on sediment cores PS1599, PS1789, and PS1791 (Sprenk et al., 2013b). Although, the varved sections of PS1795 have similar average

CPD
9, 5123–5156, 2013

grain sizes as the cores studied previously, the seasonal differences are subdued, the X-radiographs do not show the differences accordingly (Fig. 4) and the layers cannot always be adequately counted. To obtain more information on the texture and composition of the individual layers as well as to better understand the seasonal sedimentation process, we produced thin sections of the varved sediment.

4.3.1 Thin sections

Figure 4 shows that the scanned images of the thin sections provide more detailed information of the internal structure and composition of the varves. Strong thickness variations can be noticed both in the brown-coloured clayey layers and the light-coloured silty layers (Fig. 3), with thicknesses of only few hundred µm up to 3 mm. There are only smaller variations in grain size and no erosional or sharp bases. Both findings argue against turbiditic deposition and favour varve formation (Fig. 3a). Sand and coarse-silt contents may vary significantly between individual layers. However, some parts of the record reveal very little difference in grain size so that individual layers are hardly recognisable in thin sections (Fig. 3) and cannot be distinguished on X-radiographs (Fig. 4) at all. Some layers are completely IRD-free (Fig. 3b), while others contain high amounts of sand-size grains (Fig. 3c). IRD appears to be mainly embedded in the lighter silty layers. Figure 4d shows some large IRD – up to 2 mm in diameter – deforming the underlying layers. This is a clear indication that either icebergs or sea ice transported the IRD and deposited it by dropping onto the sea floor.

4.3.2 Element composition

To investigate elemental composition changes, we scanned the sediment slabs prepared for thin sections (see Methods) every 0.2 mm (Fig. 4). Additionally, three archive halves were scanned for XRF at high resolution. Due to the fact that the varves are not exactly horizontally orientated and the radiographs, taken from a different part of the sediment as the XRF-scanner data were measured, both data sets do not reflect the

CPD
9, 5123–5156, 2013

same position in the sediment at the same depth. Therefore, we shifted the complete XRF-data curves a few millimetres (Fig. 5) in order to align them. Accordingly, most parts of Fig. 5 show a good correlation between XRF-derived elemental counts and the grey value curve estimated from X-radiographs, roughly reflecting density changes of the material. The most meaningful variation of elements in varved sediment are displayed in Figs. 4 and 5 and described in the following chapters. Characteristics of the clayey and silty layers are also highlighted in Table 2.

Si can either be of detrital or biogenic origin, i.e. bounded in biogenic opal (Sprenk et al., 2013a). Given that the biogenic opal content of the glacial varves (Fig. 2k; Sect. 4.1) of PS1795 is less than 5 %, with a mean of 2.2 %, Si is mostly of detrital origin. Analyses of the coarse-grained fraction also revealed that, on average, about 80 % of the particles coarser than 63 µm are actually quartz grains. The combination of thin sections and XRF-data (Fig. 4) highlights that Si counts are relatively enriched in coarser, light-coloured layers relative to brownish clayey layers. This indicates that Si counts every 0.2 mm can be an ideal additional tool for detrital varve counting. Figure 5 shows that the overall amount of Si also correlates to grey values derived from radiographs, which are positively correlated to sediment density (see methods). Si counts are also a good indicator for facies changes (see Fig. 2). Si counts are significantly lower in bioturbated sections relative to varved sections, due to increased water content of the sediment.

Potassium (K), iron (Fe), and titanium (Ti) show strong positive correlation, which is reflected in the Ti/Fe ratio of $r^2 = 0.84$ and K/Ti ratio of $r^2 = 0.90$. This suggests that K, Fe, and Ti are mainly bounded in clay minerals such as the chlorite and illite groups as well as mica biotite. Figure 4 highlights that K, Fe, and Ti show maxima in brownish coloured clayey layers.

Rubidium (Rb) has a similar ionic radius as K. Therefore, it commonly replaces it and can often be detected in K-feldspars, mica, and clay minerals (Chang et al., 2013). Cu, Zn, Rb, Cs, Ba, and Sn are generally related to clay minerals (Vital and Stattegger, 2000). Fine-grained sediments show typically high Rb counts (Dypvik and Har-

CPD
9, 5123–5156, 2013

ris, 2001), which is also documented in varved sections of PS1795, where Rb is like K, Fe, and Ti enriched in clayey layers (Fig. 4).

Strontium (Sr) has an atomic radius similar to calcium (Ca) and can therefore replace it easily. Both elements are slightly enriched in siltier layers (Fig. 4). Ca and Si show a good correlation with a coefficient of $r^2 = 0.78$.

Zirconium (Zr) is comparatively immobile, mainly residing in heavy minerals, e.g. zircon, resistant to chemical as well as physical weathering (Wayne Nesbitt and Markovics, 1997; Alfonso et al., 2006). Thus Zr is mainly transported with coarser particles (Vogel et al., 2010). Zr shows maxima mainly in coarser silty layers. Comparing the scanned thin sections and the Zr counts (Fig. 4), reveals that especially thicker and coarser silty layers have maxima in Zr counts.

4.3.3 RADIUS tool

To gain more information on the particles and their size distribution in varved layers, we applied the particle analysing RADIUS tool (Seelos, 2004) on high-resolution, scanned thin sections. The RADIUS tool differentiates between (i) bright particles, i.e. mainly quartz, and light feldspars, (ii) dark particles, i.e. opaque minerals, and (iii) carbonates (Seelos and Sirocko, 2005). Carbonate particles are neglected in Fig. 6 given that the values are extremely low and not significant, which is also reflected in the low TIC content of varved sediment (Fig. 2).

Figure 6 shows the percentage of detected bright and dark particles in the grain size fraction 20–63 µm, i.e. medium to coarse silt, of total grains (i.e. of all classified grains up to 200 µm in diameter). In lighter layers, bright silt-sized particles have local maxima and are accounting for up to 10 % of the total grains. Also, the mean size of the bright particles is mostly higher in lighter layers than in brown layers (Fig. 6). Although, single IRD, e.g. at 368.5 or 369 cm, strongly influence the mean particle size. The median size of bright particles is about 34 µm. In contrast to that, dark particles have only median sizes of about 22 µm. This is also reflected in the overall low content of dark particles in the medium to coarse silt fraction with only up to 1.2 % of all classified grains and

CPD
9, 5123–5156, 2013

yet in some parts even no detected dark particles. The correlation of the silt-sized dark particles and the sediment layers is not as striking as for the bright particles (Fig. 6). However, many lighter layers also show increased amounts in silt-sized as well as higher mean size of dark particles.

5 Discussion

5.1 Seasonal sedimentation changes

Our age model relying on ^{14}C dates and varve counting reveals that the varved sediment was deposited during the LGM, when the ice sheets in the Weddell Sea area had most likely advanced to the shelf break (e.g. Weber et al., 2011; Hillenbrand et al., 2012). The estimated linear sedimentation rate of about 1.1–1.6 m kyr^{-1} for the varved sediment of PS1795 (e.g. Fig. 6), is somewhat lower than established for core sites farther downslope on the same channel-ridge system. Sprenk et al. (2013b) calculated mean linear sedimentation rates from varve counting varying between 2.2 and 5.3 m kyr^{-1} for the cores PS1599, PS1789, and PS1791 (Fig. 1). The differences in sedimentation rates are possibly related to the location of the core sites. In contrast to the earlier investigated core sites located on the sediment ridges NW of the channels, PS1795 originates from a shallower position farther southwest outside the channel, on a steeper part of the continental slope (Fig. 1) where the channel-ridge system starts to develop.

The main differences of the layers come from seasonal changes in grain size and related changes in element and mineral composition (Table 2). The lighter-coloured layers show maxima in the amount of bright particles, mainly quartz in the medium to coarse silt grain size (Fig. 6), which is also reflected in Si count maxima (Figs. 4,5). The lighter-coloured layers shows also slightly increased amounts of silt-sized dark particles. Enriched Zr counts in the silty layers also allude to coarser grain-sized material besides higher densities indicated by less darkening of the X-ray film (Fig. 4). Interest-

CPD
9, 5123–5156, 2013

ingly, most of the IRD is included in the lighter layers (Fig. 3). The brownish-coloured layers are characterized by predominant clay-sized particles and related minerals like mica, clay minerals like e.g. chlorite and illite group members, also indicated by maxima in Fe, Ti, Rb, and K counts (Figs. 4,5).

5.2 Modern and LGM polynyas and their relation to bottom-water production in the Weddell Sea

Today, Antarctic coastal polynyas are very important areas for AABW production and therefore, polynyas also contribute to the maintenance of the overturning circulation in the oceans (Morales Maqueda et al., 2004). Offshore blowing katabatic winds remove sea ice from coastal areas or the shelf-ice edge and often implement the development of coastal polynyas (Kern, 2009; Williams et al., 2007). Open water areas form where heat from the ocean can be released to the cold atmosphere and sea-ice production is intensified leading to brine rejection and thus dense water formation (Tamura et al., 2008). Haid and Timmermann (2013) identified the Brunt Ice Shelf, which is close to the core sites (Fig. 1), together with the Ronne Ice Shelf (e.g. Hollands et al., 2013) and southern regions of Antarctic Peninsula as important polynya areas and highlighted that ice production is 9–14 times higher in these areas compared to neighbouring regions with the highest mean heat flux during the winter months July and August. Today, coastal polynyas are pervasive around Antarctica during winter (Kern, 2009) and considered as the areas of highest ice production in winter (Morales Maqueda et al., 2004). Tamura et al. (2008) estimated that 10 % of all sea ice in the Southern Ocean and about 6 % in the Weddell Sea (Renfrew et al., 2002) is produced in Antarctic coastal polynyas. In the Weddell Sea, investigations showed that years with large coastal polynya areas are in accordance with maxima in total ice extent (Comiso and Gordon, 1998). Renfrew et al. (2002) highlighted that the inter-annual variations in coastal polynya activity and area seem to be related to katabatic winds, cyclones, as well as barrier winds.

Heinemann et al. (2013) studied coastal polynyas in the Weddell Sea area and showed that in the area of Coats Land, in front of the Brunt Ice Shelf (Fig. 1), the

CPD
9, 5123–5156, 2013

offshore winds are mainly driven by katabatic winds, due to the steepness and length of the slope. However, for glacial conditions, there is still little knowledge on katabatic winds and coastal polynya activity as well as their seasonal changes in the southeastern Weddell Sea. Due to the fact that ice sheets covered the continental shelf in the Weddell Sea, the bottom-water formation must have deviated from today, where dense bottom waters are formed on the continental shelf under the ice shelves (e.g. Haid and Timmermann, 2013). LGM simulations by Shin et al. (2003) showed that around 80 % of the AABW could have been formed by increased brine release in the sea-ice production zones in the Southern Ocean. Coastal polynyas in front of the grounded ice sheet above the continental slope might have played a major role in the bottom water formation during the LGM. Earlier studies (e.g. Weber et al., 1994, 2011; Sprenk et al., 2013b) indicated that during the LGM intensified katabatic winds likely drove coastal polynya formation in the southeastern Weddell Sea. Smith et al. (2010) also pointed out that during the last glacial, off-blowing katabatic winds in front of the grounded Antarctica Peninsula Ice Sheet formed coastal polynyas in the Western Weddell Sea.

The Weddell Sea varves were deposited only during glacial times when the grounded ice sheet had very likely advanced to the shelf break (e.g. Hillenbrand et al., 2012). Based on earlier (e.g. Weber et al., 1994; Kuhn and Weber, 1993; Sprenk et al., 2013b) as well as on this study, we favour the following scenario of glacial sedimentation: during the LGM, plumes of cold and dense water were generated in front of the grounded East Antarctic Ice Sheet above the upper slope by coastal polynya, i.e. operated by strong offshore blowing (i.e. katabatic) winds enhancing sea-ice formation and thus brine release. The resulting dense water mass moved down the continental slope and was canalized into the channel-ridge systems northeast of Crary Fan (Fig. 1), producing cold and saline WSBW. Apparently, this flow oscillated seasonally with a stronger salt injection during glacial winter due to increased brine release by more intense coastal polynya. We should note that spaces of open water, which were generated by the katabatic winds and led to glacial polynyas did likely not stay open for long because of the low temperatures. Rapid freezing and associated intense brine

CPD
9, 5123–5156, 2013

rejection should therefore be a major difference to present-day polynyas, which may stay open for longer and do therefore not invoke major brine rejection. The resulting glacial thermohaline current flowed underneath and against the probably weakened Weddell Gyre. The clayey layer would hence have be interpreted as a summer signal, resulting from less intense katabatic winds, hence less sea-ice transport away from the coast, reduced brine rejection in front of the ice sheet that led to reduced thermohaline convection, lower current velocities in the channels, and less overspilling on the ridges. Vice versa, coarser-grained silty layer should represent a winter signal as a result of enhanced katabatic winds that carried sea ice away from the continent more effectively, inducing rapid freezing processes at the surface that spurred thermohaline convection, led higher velocities in the channels and higher overspilling on the ridges. As a whole, the seasonally variable thermohaline convection produced large volumes of bottom water and transported vast amounts of sediment into the deeper environment that have originally been delivered by meltwater channels from the grounded ice sheet and/or by gravitational processes (Anderson et al., 1986), leaving its trace in form of varved sediment on the ridges (Figs. 3–5). In a coupled climate model, Justino and Peltier (2006) demonstrated that the seasonal cycle in the Southern Ocean was likely much stronger during LGM than it is today with a very pronounced winter season. Since coastal polynya formation is mainly driven by the intensity of the katabatic winds, sea-ice was moved away from the continent and/or thinned close to the coast in glacial winter, allowing for a more intense transport of icebergs counter clockwise around Antarctica within the Antarctic Coastal Current. This could explain why coarser-grained (winter) layers occur preferentially with higher amounts of IRD.

Alternatively, coarser layers could have been deposited during summer, when ice melt occurred more likely. This interpretation could be supported by the fact that the silty layers contain higher IRD contents resulting from ice melt. Ice melt could occur either through direct surface melt, although modelling of atmospheric teleconnections from sea-surface temperature variations from equatorial Pacific (Weber et al., 2011) show that increasing temperatures would not lead to a negative ice mass balance un-

CPD
9, 5123–5156, 2013

der LGM conditions. Meltwater could also be delivered by meltwater channels directly from the ice sheet. That process, however would only deliver fresh water that is not dense enough to sink down and move across the shelf and onto the continental slope and into the channels that accompany the ridges because the surrounding brines are much denser. Also, seasonal deposition on the ridges requires a continuous flow of a dense water mass at varying volume (velocity) in the channels that is deflected to the left due to the influence of Coriolis Force, and overspills the channels on their northwestern side. This process can most likely only be sustained by a seasonally variable thermohaline convection resulting from polynya formation in front of the ice edge. Nonetheless, there is no definitive interpretation possible at the current stage as to which season produced which layer.

6 Conclusions

We presented high-resolution sediment-physical and geochemical data of the newly opened sediment core PS1795 from a channel-ridge system located on a terrace of the continental slope of the southeastern Weddell Sea. ^{14}C ages and varve counting results for PS1795 underline earlier studies that laminations represent true varves and are therefore seasonally deposited during the LGM with sedimentation rates of about 1.1–1.6 m kyr^{-1}. Thin sections, XRF-scanning at 0.2 mm resolution, as well as RADIUS tool analysis reveal detailed information on the internal varve composition. Individual layers have thicknesses of only few hundred µm up to 3 mm. The facts that laminae couplets show only small variations in grain size and there are no erosional or sharp surfaces argues against turbiditic sedimentation and favours varve formation. In fact, grain-size variability of some parts is so low that layers are hardly be distinguishable in thin sections cannot be recognised on X-radiographs at all. Analyses of thin sections show that IRD is mainly embedded in the lighter, silty layers with some large debris – up to 2 mm in diameter – deforming the underlying layers. This is a clear indication of transport by either icebergs or sea ice, and deposition by dropping onto the sea floor.

CPD
9, 5123–5156, 2013

Our results reveal seasonal changes in grain size and related changes in element and mineral composition. Lighter-coloured layers contain higher amounts of silt-sized particles, mostly quartz grains, which is also shown by maxima in Si counts. Light layers are also enriched in Zr, reveal coarser grain sizes and show higher densities as indicated by less darkening of the X-ray film. Finer grained layers are of darker colour, contain mainly clay-sized particles as well as maxima in K, Fe, Ti, and Rb, i.e. typical trace elements for clay minerals such as chlorite and illite as well as mica such as biotite.

Consequently, sedimentation in the channel-ridge-system was highly dynamic during the LGM, reflecting seasonal velocity changes of the thermohaline current that transporting sediment from the upper slope downslope to the core sites. Sediments were deposited when the grounded ice sheet had advanced to the Weddell Sea shelf edge. Offshore blowing katabatic winds removed sea ice from the ice edge and coastal polynyas developed. We suggest that glacial coastal polynya processes were in general similar to today inasmuch as stronger katabatic winds and enhanced coastal polynya activity occurred during the winter season. However, that does not imply the spaces of open water may have existed for long. Following this concept, silty layers are likely glacial winter deposits, when brine release was increased leading to intensified bottom water formation and increased sediment transport. Vice versa, finer-grained clayey layers were deposited during summer, when coastal polynya activity was possibly reduced.

Nonetheless, there is currently no concluding interpretation as to which season produced which layer. Coarser layers could also have been deposited during glacial summer by meltwater channels or when more sea ice melted, which might also explain the higher IRD content in silty layers. However, the density of melted freshwater would have been too low to sink down the continental slope and initiate the required thermohaline circulation.

Acknowledgements. The authors are grateful for financial support from the Deutsche Forschungsgemeinschaft (DFG; grants RI 525/17-1, KU 683/9-1, WE2039/8-1) and the DFG-Priority Programme Antarctic Research 1158. Our study was part of the Alfred Wegener In-

CPD
9, 5123–5156, 2013

stitute research program “Polar Regions and Coasts in a changing Earth System” (PACES), Topic 3 “Lessons from the Past”. We thank Irka Hajdas from the Laboratory of Ion Beam at the ETH Zurich for the AMS^{14}C measurements as well as Ralf Baeumler and Jens Karls from the University of Cologne for helping with the thin sections. Supplementary data to this paper are available at (doi will be implemented soon).

References

Alfonso, J. A., Martínez, M., Flores, S., and Benzo, Z.: Distribution of Trace Elements in Offshore Sediments of the Orinoco Delta, J. Coastal Res., 502–510, doi:10.2112/03-0142.1, 2006.

Anderson, J. B., Wright, R., and Andrews, B.: Weddell Fan and Associated Abyssal Plain, Antarctica: Morphology, Sediment Processes, and Factors Influencing Sediment Supply, Geo-Mar. Lett., 6, 121–129, 1986.

Axelsson, V.: The use of X-ray radiographic methods in studying sedimentary properties and rates of sediment accumulation, Hydrobiologia, 103, 65–69, 1983.

Beckmann, A., Hellmer, H. H., and Timmermann, R.: A numerical model of the Weddell Sea: Large-scale circulation and water mass distribution, J. Geophys. Res.-Ocean., 104, 23375–23391, doi:10.1029/1999JC900194, 1999.

Blaauw, M.: Methods and code for “classical” age-modelling of radiocarbon sequences, Quaternary Geochronol., 5, 512–518, doi:10.1016/j.quageo.2010.01.002, 2010.

Carmack, E. C. and Foster, T. D.: Water masses and circulation in the Weddell Sea, edited by: Dumkar, M. J., 151–165, 1977.

Chang, H., An, Z., Wu, F., Jin, Z., Liu, W., and Song, Y.: A Rb/Sr record of the weathering response to environmental changes in westerly winds across the Tarim Basin in the late Miocene to the early Pleistocene, Palaeogeogr. Palaeocli., 386, 364–373, doi:10.1016/j.palaeo.2013.06.006, 2013.

Clark, P. U., Dyke, A. S., Shakun, J. D., Carlson, A. E., Clark, J., Wohlfarth, B., Mitrovica, J. X., Hostetler, S. W., and McCabe, A. M.: The Last Glacial Maximum, Science, 325, 710–714, doi:10.1126/science.1172873, 2009.

Comiso, J. C. and Gordon, A. L.: Interannual variability in summer sea ice minimum, coastal polynyas and bottom water formation in the Weddell Sea, Antarctic Res. Ser., 74, 293–315, 1998.

CPD
9, 5123–5156, 2013

Cook, T., Bradley, R., Stoner, J., and Francus, P.: Five thousand years of sediment transfer in a high arctic watershed recorded in annually laminated sediments from Lower Murray Lake, Ellesmere Island, Nunavut, Canada, J. Paleolimnol. 41, 77–94–94, doi:10.1007/s10933-008-9252-0, 2009.

Croudace, I. W., Rindby, A., and Rothwell, R. G.: ITRAX: description and evaluation of a new multi-function X-ray core scanner, Geological Society, London, Special Publications, 267, 51–63, 2006.

Dypvik, H. and Harris, N. B.: Geochemical facies analysis of fine-grained siliciclastics using Th/U, Zr/Rb and (Zr+Rb)/Sr ratios, Chem. Geol., 181, 131–146, doi:10.1016/S0009-2541(01)00278-9, 2001.

Elverhøi, A.: Glacigenic and associated marine sediments in the Weddell Sea, fjords of Spitsbergen and the Barents Sea: A review, Mar. Geol., 57, 53–88, doi:10.1016/0025-3227(84)90195-6, 1984.

Foldvik, A.: Oceanographic research during Nare-84/85, Filchner Ronne Ice Shelf Programme Rep., 3, 107–109, 1986.

Foldvik, A., Gammelsrød, T., and Tørresen, T.: Circulation and water masses on the southern Weddell Sea shelf, in: Oceanology of the Antarctic Continental Shelf, Antarct. Res. Ser., AGU, Washington, DC, 5–20, 1985.

Foldvik, A., Gammelsrød, T., Østerhus, S., Fahrbach, E., Rohardt, G., M., S., Nicholls, K. W., Padman, L., and Woodgate, R. A.: Ice shelf water overflow and bottom water formation in the southern Weddell Sea, J. Geophys. Res., 109, C02015, doi:10.1029/2003JC002008, 2004.

Francus, P. and Asikainen, C. A.: Sub-sampling unconsolidated sediments: A solution for the preparation of undistrubed thin-sections from clay-rich sediments, J. Paleolimnol., 26, 323–326, doi:10.1023/A:1017572602692, 2001.

Gales, J. A., Larter, R. D., Mitchell, N. C., Hillenbrand, C. D., Østerhus, S., and Shoosmith, D. R.: Southern Weddell Sea shelf edge geomorphology: Implications for gully formation by the overflow of high-salinity water, J. Geophys. Res., 117, F04021, doi:10.1029/2012JF002357, 2012.

Gleissberg, W.: A table of secular variations of the solar cycle, Terr. Magn. Atmos. Electr., 49, 243–244, 1944.

Gleissberg, W.: The eighty-year sunspot cycle, J. Br. Astron. Assoc., 68, 148–152, 1958.

Gordon, A. L., Huber, B., McKee, D., and Visbeck, M.: A seasonal cycle in the export of bottom water from the Weddell Sea, Nat. Geosci., 3, 551–556, doi:10.1038/NGEO916, 2010.

CPD
9, 5123–5156, 2013

Grobe, H.: A simple method for the determination of ice-rafted debris in sediment cores, Polarforschung, 57, 123–126, 1987.
Haid, V. and Timmermann, R.: Simulated heat flux and sea ice production at coastal polynyas in the southwestern Weddell Sea, J. Geophys. Res.-Ocean., 118, 2640–2652, doi:10.1002/jgrc.20133, 2013.
Heinemann, G., Ebner, L., Haid, V., and Timmermann, R.: Katabatic winds and polynya dynamics in the Weddell Sea region (Antarctica), EGU General Assembly 2013, Vienna, 2013.
Hillenbrand, C.-D., Melles, M., Kuhn, G., and Larter, R. D.: Marine geological constraints for the grounding-line position of the Antarctic Ice Sheet on the southern Weddell Sea shelf at the Last Glacial Maximum, Quaternary Sci. Rev., 32, 25–47, doi:10.1016/j.quascirev.2011.11.017, 2012.
Hollands, T., Haid, V., Dierking, W., Timmermann, R., and Ebner, L.: Sea ice motion and open water area at the Ronne Polynia, Antarctica: Synthetic aperture radar observations versus model results, J. Geophys. Res.-Ocean., 118, 1940–1954, doi:10.1002/jgrc.20158, 2013.
Huhn, O., Hellmer, H. H., Rhein, M., Rodehacke, C., Roether, W., Schodlok, M. P., and Schroeder, M.: Evidence of deep- and bottom-water formation in the western Weddell Sea, Deep-Sea Res. Part II, 55, 1098–1116, doi:10.1016/j.dsr2.2007.12.015, 2008.
Jansen, J. H. F., Van der Gaast, S. J., Koster, B., and Vaars, A. J.: CORTEX, a shipboard XRF-scanner for element analyses in split sediment cores, Mar. Geol., 151, 143–153, doi:10.1016/s0025-3227(98)00074-7, 1998.
Justino, F. and Peltier, W. R.: Influence of present day and glacial surface conditions on the Antarctic Oscillation/Southern Annular Mode, Geophys. Res. Lett., 33, L22702, doi:10.1029/2006GL027001, 2006.
Kern, S.: Wintertime Antarctic coastal polynya area: 1992–2008, Geophys. Res. Lett., 36, L14501, doi:10.1029/2009GL038062, 2009.
Knutti, R., Flückiger, J., Stocker, T. F., and Timmermann, A.: Strong hemispheric coupling of glacial climate through freshwater discharge and ocean circulation, Nature, 430, 851–856, 2004.
Kuhn, G. and Weber, M. E.: Acoustical characterization of sediments by Parasound and 3.5 kHz systems: Related sedimentary processes on the southeastern Weddell Sea continental slope, Antarctica, Mar. Geol., 113, 201–217, 1993.
Larter, R. D., Graham, A. G. C., Hillenbrand, C.-D., Smith, J. A., and Gales, J. A.: Late Quaternary grounded ice extent in the Filchner Trough, Weddell Sea, Antarctica: new marine geo-

CPD
9, 5123–5156, 2013

physical evidence, Quaternary Sci. Rev., 53, 111–122, doi:10.1016/j.quascirev.2012.08.006, 2012.
Maldonado, A., Barnolas, A., Bohoyo, F., Escutia, C., Galindo-Zaldívar, J., Hernández-Molina, J., Jabaloy, A., Lobo, F. J., Nelson, C. H., Rodríguez-Fernández, J., Somoza, L., and Vázquez, J.-T.: Miocene to Recent contourite drifts development in the northern Weddell Sea (Antarctica), Global Planet. Change, 45, 99–129, doi:10.1016/j.gloplacha.2004.09.013, 2005.
Melles, M.: Paläoglaziologie und Paläozeanographie im Spätquartär am Kontinentalrand des südlichen Weddellmeeres, Antarktis, Ber. Polarforsch., 1991.
Michels, K. H., Kuhn, G., Hillenbrand, C.-D., Diekmann, B., Fütterer, D. K., Grobe, H., and Uenzelmann-Neben, G.: The southern Weddell Sea: combined contourite-turbidite sedimentation at the southeastern margin of the Weddell Gyre, Geol. Soc. Memoirs, 22, 305–323, 2002.
Morales Maqueda, M. A., Willmott, A. J., and Biggs, N. R. T.: Polynya dynamics: A review of observations and modeling, Rev. Geophys., 42, RG1004, doi:10.1029/2002RG000116, 2004.
Müller, P. J. and Schneider, R.: An automated leaching method for the determination of opal in sediments and particulate matter, Deep-Sea Res. I, 40, 425–444, 1993.
Nicholls, K. W., Østerhus, S., Makinson, K., Gammelsrød, T., and Fahrbach, E.: Ice-ocean processes over the continental shelf of the southern Weddell Sea, Antarctica: A review, Rev. Geophys., 47, RG3003, doi:10.1029/2007RG000250, 2009.
Orsi, A. H., Nowlin jr, W. D., and Whitworth III, T.: On the circulation and stratification of the Weddell Gyre, Deep-Sea Res. I, 40, 169–203, 1993.
Orsi, A. H., Johnson, G. C., and Bullister, J. L.: Circulation, mixing, and production of Antarctic Bottom Water, Progr. Oceanogr., 43, 55–109, doi:10.1016/s0079-6611(99)00004-x, 1999.
Petty, A. A., Feltham, D. L., and Holland, P. R.: Impact of Atmospheric Forcing on Antarctic Continental Shelf Water Masses, J. Phys. Oceanogr., 43, 920–940, doi:10.1175/JPO-D-12-0172.1, 2013.
Rahmstorf, S.: Ocean circulation and climate during the past 120,000 years, Nature, 419, 207–214, 2002.
Reimer, P. J., Baillie, M. G. L., Bard, E., Bayliss, A., Beck, J. W., Blackwell, P. G., Ramsey, C. B., Buck, C. E., Burr, G. S., Edwards, R. L., Friedrich, M., Grootes, P. M., Guilderson, T. P., Hajdas, I., Heaton, T. J., Hogg, A. G., Hughen, K. A., Kaiser, K. F., Kromer, B., McCormac,

CPD
9, 5123–5156, 2013

F. G., Manning, S. W., Reimer, R. W., Richards, D. A., Southon, J. R., Talamo, S., Turney, C. S. M., van der Plicht, J., and Weyhenmeyer, C. E.: IntCal09 and Marine09 Radiocarbon Age Calibration Curves, 0–50,000 Years cal BP, Radiocarbon, 51, 1111–1150, 2011.

Renfrew, I. A., King, J. C., and Markus, T.: Coastal polynyas in the southern Weddell Sea: Variability of the surface energy budget, J. Geophys. Res., 107, 3063, doi:10.1029/2000jc000720, 2002.

Seelos, K.: Entwicklung einer numerischen Partikelanalyse-Methode auf Basis digitaler Dünnschliffaufnahmen und Anwendung der Routine auf die ELSA-HL2- Kernsequenz 66-41 m, Doktor, Institut für Geowissenschaften, Johannes Gutenberg-Universität, Mainz, 1–171, 2004.

Seelos, K. and Sirocko, F.: RADIUS – rapid particle analysis of digital images by ultra-high-resolution scanning of thin sections, Sedimentology, 52, 669–681, 2005.

Seidov, D., Barron, E., and Haupt, B. J.: Meltwater and the global ocean conveyor: northern versus southern connections, Global Planet. Change, 30, 257–270, 2001.

Shin, S.-I., Liu, Z., Otto-Bliesner, B. L., Kutzbach, J. E., and Vavrus, S. J.: Southern Ocean sea-ice control of the glacial North Atlantic thermohaline circulation, Geophys. Res. Lett., 30, 6861–6864, doi:10.1029/2002GL015513, 2003.

Smith, J. A., Hillenbrand, C.-D., Pudsey, C. J., Allen, C. S., and Graham, A. G. C.: The presence of polynyas in the Weddell Sea during the Last Glacial Period with implications for the reconstruction of sea-ice limits and ice sheet history, Earth Planet. Sci. Lett., 296, 287–298, doi:10.1016/j.epsl.2010.05.008, 2010.

Sprenk, D., Weber, M. E., Kuhn, G., Rosén, P., Frank, M., Molina-Kescher, M., Liebetrau, V., and Röhling, H.-G.: Southern Ocean bioproductivity during the last glacial cycle – new decadal-scale insight from the Scotia Sea, Geological Society, London, Special Publications, 381, doi:10.1144/SP381.17, 2013a.

Sprenk, D., Weber, M. E., Kuhn, G., Prange, M., Varma, V., and Schulz, M.: Decadal- to millennial-scale oscillations in the Weddell Sea during the Last Glacial Maximum, Quaternary Sci. Rev., in review, 2013b.

Stocker, T. F. and Johnson, S. J.: A minimum thermodynamic model for the bipolar seesaw, Paleoceanography, 18, 1087–1095, 2003.

Tamura, T., Ohshima, K. I., and Nihashi, S.: Mapping of sea ice production for Antarctic coastal polynyas, Geophys. Res. Lett., 35, L07606, doi:10.1029/2007GL032903, 2008.

CPD
9, 5123–5156, 2013

Vital, H. and Stattegger, K.: Major and trace elements of stream sediments from the lowermost Amazon River, Chem. Geol., 168, 151–168, doi:10.1016/S0009-2541(00)00191-1, 2000.
Vogel, H., Wagner, B., Zanchetta, G., Sulpizio, R., and Rosén, P.: A paleoclimate record with tephrochronological age control for the last glacial-interglacial cycle from Lake Ohrid, Albania and Macedonia, J. Paleolimnol., 44, 295–310, 2010.
Wayne Nesbitt, H. and Markovics, G.: Weathering of granodioritic crust, long-term storage of elements in weathering profiles, and petrogenesis of siliciclastic sediments, Geochim. Cosmochim. Acta, 61, 1653–1670, doi:10.1016/S0016-7037(97)00031-8, 1997.
Weber, M. E.: Estimation of biogenic carbonate and opal by continuous non-destructive measurements in deep-sea sediments: application to the eastern Equatorial Pacific, Deep-Sea Res., 1, 45, 1955-1975, doi:10.1016/S0967-0637(98)00028-4, 1998.
Weber, M. E., Bonani, G., and Fütterer, K. D.: Sedimentation processes within channel-ridge systems, southeastern Wedell Sea, Antarctica, Paleoceanography, 9, 1027–1048, 1994.
Weber, M. E., Niessen, F., Kuhn, G., and Wiedicke, M.: Calibration and application of marine sedimentary physical properties using a multi-sensor core logger, Mar. Geol., 136, 151–172, doi:10.1016/S0025-3227(96)00071-0, 1997.
Weber, M. E., Reichelt, L., Kuhn, G., Pfeiffer, M., Korff, B., Thurow, J., and Ricken, W.: BMPix and PEAK tools: New methods for automated laminae recognition and counting—Application to glacial varves from Antarctic marine sediment, Geochem. Geophys. Geosyst., 11, 1–18, doi:10.1029/2009GC002611, 2010.
Weber, M. E., Clark, P. U., Ricken, W., Mitrovica, J. X., Hostetler, S. W., and Kuhn, G.: Interhemispheric Ice-Sheet Synchronicity During the Last Glacial Maximum, Science, 334, 1265–1269, doi:10.1126/science.1209299, 2011.
Williams, W. J., Carmack, E. C., and Ingram, R. G.: Chapter 2 Physical Oceanography of Polynyas, in: Elsevier Oceanography Series, edited by: Smith, W. O. and Barber, D. G., Elsevier, 55–85, 2007.

CPD
9, 5123–5156, 2013

Table 1. Accelerator mass spectrometry (AMS) ^{14}C ages measured on planktonic foraminifera *Neogloboquadrina pachyderma* shells at the ETH laboratory of Ion Beam Physics in Zurich. Also the amount of C used for each measurement is included in the table. AMS ^{14}C ages were reservoir corrected (1215 ± 30 yr), based on age dating of carbonate shell material from a living bryozoa from neighbouring Site PS1418-1 (Melles, 1991). Clam 2.1 (Blaauw, 2010) and the Marine09 calibration curve (Reimer et al., 2011) were used to calculate calendar years before present (cal yr BP). For all ages also the estimated error of the dating method is given.

Laboratory code	Sample depth (cm)	Amount C (mg)	Uncalibrated ^{14}C age (yr BP) ± error	Age min (cal yr BP)	Age max (cal yr BP)	Probab. (%)
ETH-48371	210–215	0,23*	15947 ± 77	17 087	17 797	95
ETH-48372	390–415	0,38*	22 211 ± 86	24 304	24 946	95
ETH-48373	450	0,87	20 501 ± 60	22 221	22 678	83.9
ETH-48373	450	0,87	20 501 ± 60	22 764	22 950	8
ETH-48373	450	0,87	20 501 ± 60	23 140	23 229	3.1
ETH-48374	655–680	0,31*	21 912 ± 90	23 903	24 474	95
ETH-48375	775–795	0,42	21 546 ± 80	23 437	24 170	95
ETH-48376	865–880	0,54	21 643 ± 77	23 558	24 289	95

CPD
9, 5123–5156, 2013

Table 2. Characteristics of seasonally deposited clayey and silty layers. Elements were measured using ITRAX X-ray fluorescence scanner (see also Figs. 4–6).

Characteristics	Clayey layer	Silty layer
Colour	brown	light-coloured
Si, Ca, Sr, Zr	low	high
K, Ti, Fe, Rb	high	low
Grey value	low	high
Silt-sized bright particles	low	high
Silt/fine sand content	low	high
Ice-rafted debris	low	high
Bottom current velocity	low	high

CPD
9, 5123–5156, 2013

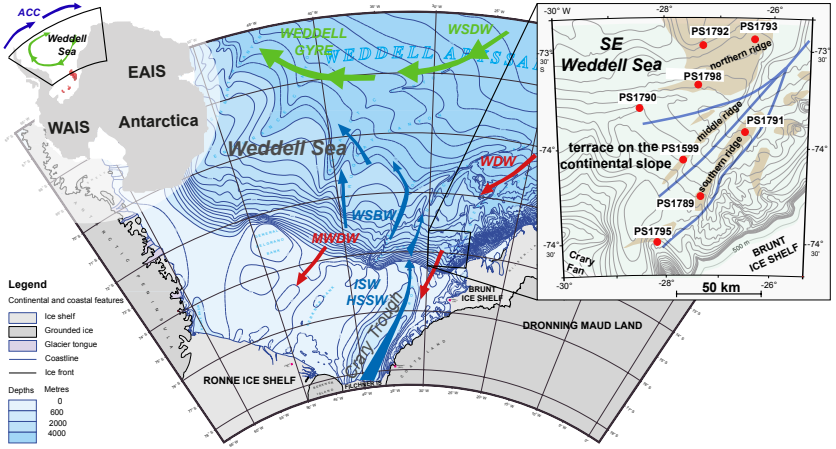

Fig. 1. On the left side is an overview map showing whole Antarctica with the West (WAIS) and East (EAIS) Antarctic Ice Sheets as well as Antarctic Peninsula. The Weddell Sea (black square) is located in the southernmost part of Atlantic sector of the Southern Ocean. Additionally, the clockwise flowing Antarctic Circumpolar Current (ACC) and the Weddell Gyre (green arrows) are highlighted. The map in the centre shows a bathymetric chart of the Weddell Sea (Alfred Wegener Institute for Polar and Marine Research BCWS 1 : 3 000 000; Bremerhaven, 1997). Present-days flow direction of important water masses, i.e. High Salinity Shelf Water (HSSW), Ice Shelf Water (ISW), Weddell Sea Bottom Water (WSBW), Warm Deep Water (WDW) and the through heat loss Modified WDW (MWDW) are indicated (further information see Sect. 2.2). The core site area (black square) is located in the southeastern Weddell Sea close to the Brunt Ice Shelf. The small map on the right is a bathymetric map focussing on the southeastern Weddell Sea modified after (Weber et al., 1994) highlighting the Polarstern (PS) core sites referred to in this study (red dots). The core sites are located on ridges on a terrace of the continental slope. Southeast of each ridge (brown colour) runs a channel. During the LGM the thermohaline current (blue lines) was flowing towards the NE in the channels. Due to the Coriolis force most of the transported sediment is deposited NW of each channel.

CPD
9, 5123–5156, 2013

Seasonal changes in glacial polynya activity inferred from Weddell Sea varves

D. Sprenk et al.

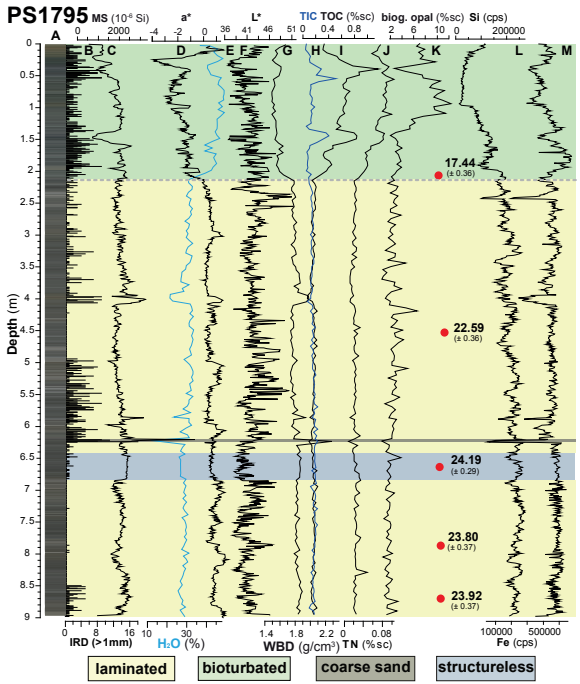

Fig. 2. Sediment-physical data from sediment core PS1795: A shows the red/green/blue (RGB) colour pattern; B shows the amounts of grains > 1 mm, representing iceberg-rafted debris (IRD; method see Grobe, 1987); C is magnetic susceptibility (MS) record; D is colour a* (green-red component); E shows the water content of the sediment; F gives lightness (L*); G is wet-bulk density (WBD); H to K are sea-salt corrected (sc) total organic and inorganic carbon (TIC/TOC), biogenic opal, and total Nitrogen (TN); L and M show chemical elements Silicon (Si), and Iron (Fe) determined with a X-ray fluorescence-scanner. ^{14}C ages (marked with red dots) measured on planktonic foraminifera *Neogloboquadrina pachyderma* are given in ka cal before present. The grey line at 2.15 m depth marks a possible hiatus (see Sect. 4.2).

CPD
9, 5123–5156, 2013

Seasonal changes in glacial polynya activity inferred from Weddell Sea varves

D. Sprenk et al.

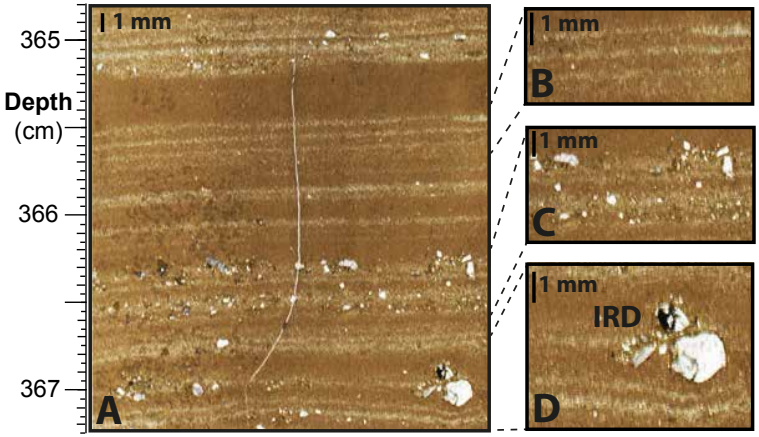

Fig. 3. Detailed images of a scanned thin section of PS1795. A gives an overview of the varved sediment and the thickness variation of silty (light-coloured) and clayey (brown-coloured) layers. On the right side are three zoomed-in photos: Regular silty-clayey-layers (B); sand-rich silty layers with some ice-rafted debris (IRD) (C); D shows some individual large IRD, deposited by deforming the sediment below.

CPD
9, 5123–5156, 2013

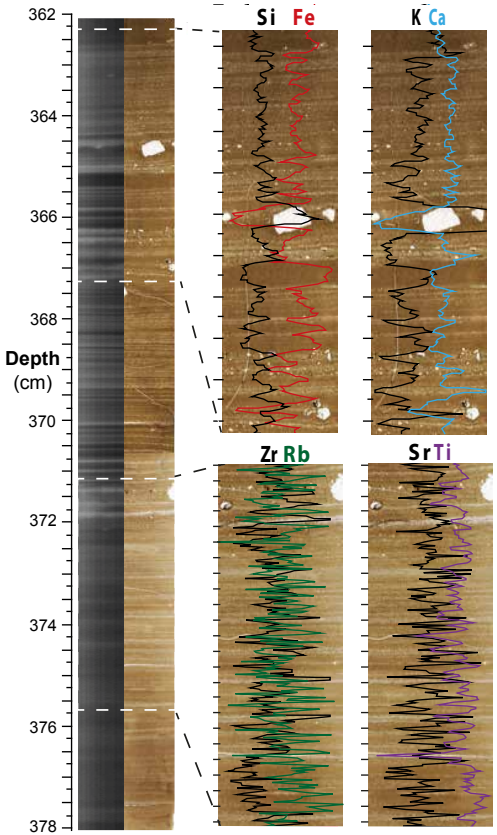

Fig. 4. High-resolution element composition of a varved sediment section of core PS1795 (362–378 cm). The left side shows X-radiographs, generated using a X-ray fluorescence (XRF) scanner and scanned images of the thin sections. On the right side are zoomed-in images of the thin sections plus XRF-scanner element counts every 0.2 mm of the sediment slabs, from which the thin sections were produced.

CPD
9, 5123–5156, 2013

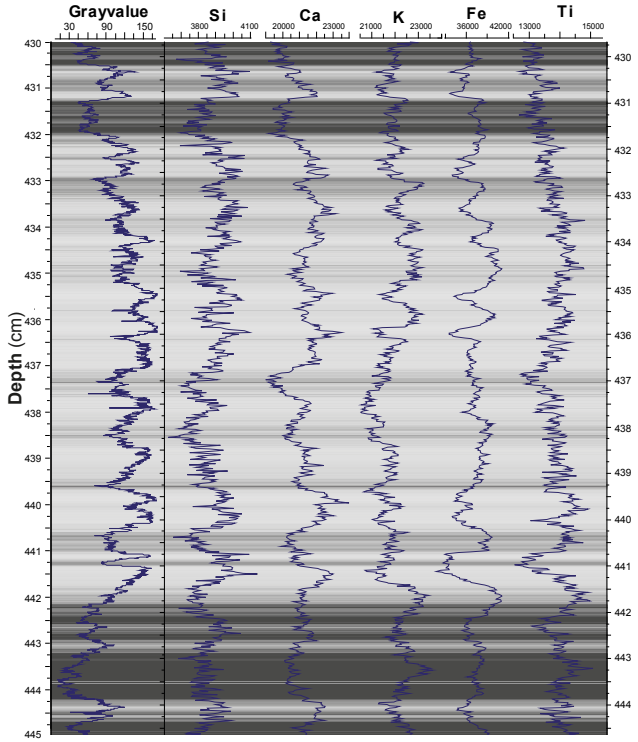

Fig. 5. Seasonal-scale changes in chemical element composition: high-resolution X-ray fluorescence scanner data (area counts) every 0.2 mm of PS1795 core section (430–445 cm). Additionally, the estimated grey scale value curve estimated from scanned X-radiograph using the BMPix tool (Weber et al., 2010) was added.

CPD
9, 5123–5156, 2013

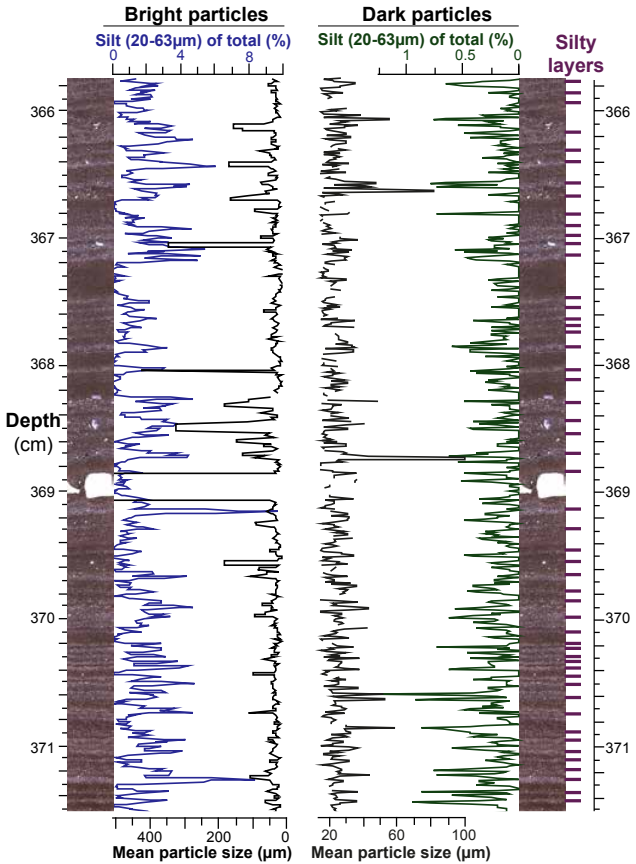

Fig. 6. Detailed particle analysis of the varved sediment section 365.8–371.5 cm with the RADIUS tool (Seelos and Sirocko, 2005) applied on high-resolution scans of the thin sections. Total refers to all analysed particle classes from 20 to 200 µm in grain size. Purple bars mark the 52 counted light-coloured silty layers leading to a resultant linear sedimentation rate of about 1.1 m kyr^{-1}.

CPD
9, 5123–5156, 2013